Draft version April 20, 2020
Typeset using LaTeX default style in AASTeX63

Planet-to-Star Radius Ratio, Transit Depth, and Transit Duration of Exoplanet Hat-P-23 b

Tyler Nill[1]

[1] *Co-Authors: Matthew Murphy, Brianna Isola, Stony Brook University, Stony Brook, NY* 11794

ABSTRACT

Exoplanet Hat-P-23 b was observed transiting its host star on September 18, 2019. Using data reduction and analysis, the transit depth, planet-to-star radius ratio, and transit duration were found. The transit depth came out to be 1.27 % ± 0.0510 %. This measurement has a significance level of 1.75σ compared to Bakos et al. (2011)'s value of 1.36 % ± 0.00700 %, and a significance level of 3.69σ compared to Tsantaki et al. (2014)'s value of 1.46 % ± 0.00700 %. The planet-to-star radius ratio came out to be 0.113 ± 0.00200, which has a significance level of 1.79σ compared to Bakos et al. (2011)'s value of 0.117 ± 0.00100, and a significance level of 2.79σ compared to Tsantaki et al. (2014)'s value of 0.1209 ± 0.00200. The transit duration came out to be 6671 seconds ± 424.3 seconds. This measurement has significance levels of 2.74σ and 1.00σ compared to Bakos et al. (2011)'s value of 7845 seconds ± 60.48 seconds and Tsantaki et al. (2014)'s value of 7102 seconds ± 69.12 seconds, respectively. All of our measurements were consistent with literature values and within 3σ besides the transit depth measurement compared to Tsantaki et al. (2014)'s value.

1. INTRODUCTION

When looking at the night sky, humans have always wondered what was out there. Astronomers have been trying to solve this problem ever since the first telescope was created. One branch of Astronomy that tries to solve this problem is the detection of extrasolar planets. Extrasolar planets, or exoplanets, are planets outside of our solar system. There are a few methods for detecting exoplanets; however, the method that was used in this experiment was the transit technique.

The transit technique was implemented by (Charbonneau et al. 2000) to confirm the existence of a previously discovered exoplanet through a different detection method; however, this technique is now one of the most used methods in detecting new exoplanets. The transit technique is observing a star outside our solar system and detecting a dip in the brightness of this star, indicating that a planet orbiting the star has crossed between the observer and the star (Gazak et al. 2012). Data analysis can be done by taking photometric images of the star before, during, and after the transit occurs. These images will allow us to measure the flux of the host star before, during, and after the transit. We should see a dip in the brightness as the planet crosses between the observer and host star, allowing us to gather "fundamental planet parameters" (Gazak et al. 2012) .

2. OBSERVATION

The exoplanet that was chosen for this experiment was Hat-P-23 b. This exoplanet was chosen due to the host star's position on the night sky during the Fall of 2019 so it would be observable by our 14-inch Meade LX200-ACF telescope on a Mesu-200 German Equatorial Mount (Meade 2019) and due to it's magnitude, which is around 12.4 (Bakos et al. 2011). On September 18, 2019, the exoplanet was observed by taking over 200 images through our Charged-Coupled Device (CCD) camera. The CCD camera that was used in this experiment was the SBIG STL-1001E CCD (CCD 2019). After taking these images, a few calibration steps were needed. These steps included the generation of a master flat field and a master dark image, determining the exact position of the host star on each image, measuring the flux of the host star within a certain aperture around it, and calibrating that flux data with calibration stars around the host star. Using the calibrated data, light curves were reproduced of the calibration stars and host star, and the transit depth, planet-to-star radius ratio, and transit duration were found.

3. DATA REDUCTION

On the same night of observation, a series of ten dark frames and ten flat fields were taken. Dark frames are frames that are taken when the shutter within the CCD is closed. These frames identify hot pixels and cosmic rays while the

flat fields correct the relative sensitivity of the CCD pixels to each other and identify dead pixels. To correct for these issues, the data analysis tool PyRAF was used (PyRAF 2019). Using PyRAF, a median combination of the series of ten dark frames and flat fields were created. These two files were called the master dark and master flat respectively. A median combination was used instead of an average combination of the files because the average is affected more by the outlying pixels, such as hot and dead pixels, than the median. To correct the images taken of the host star, the master dark was subtracted from each image, and from the master flat, and then the images were divided by the master flat. These corrections help nullify the affect of the outlying pixels and relative sensitivity of the CCD pixels.

Due to the movement of the sky, the star's position will vary between each of the CCD's images. To correct for this, the World Coordinate System (WCS) of each image was found by using the web service "Astronomy.net" (Astrometry 2019). Once this was completed, each image now had the Right Ascension and Declination of the host star.

The next step in calibrating each image was to identify and measure the properties of all the objects within each image. This was done by using the program "Source Extractor" (SourceExtractor 2019). This program returns properties such as flux, magnitudes, and position, where it creates a different file for each image. To find the flux of the host star for each image, both a fixed aperture and the gain of the CCD had to be set. The gain was set to 2.06, which is found in the CCD manual (CCD 2019). To set a fixed aperture, a small region around the host star had to be created through an astronomical image application called "DS9" (DS9 2019), as indicated by the small green circle seen in Fig. 1. The radius of this circle was found to be 5.3 pixels. After this was done a few times, the radius came out to be 5.0 pixels; however, Source Extractor only accepted the diameter of the circle rather than the radius. So, the aperture was set to 10.0 pixels within Source Extractor and Source Extractor was run on all of the host star's images. These Source Extractor files were concatenated to create a table of time, flux, and flux error.

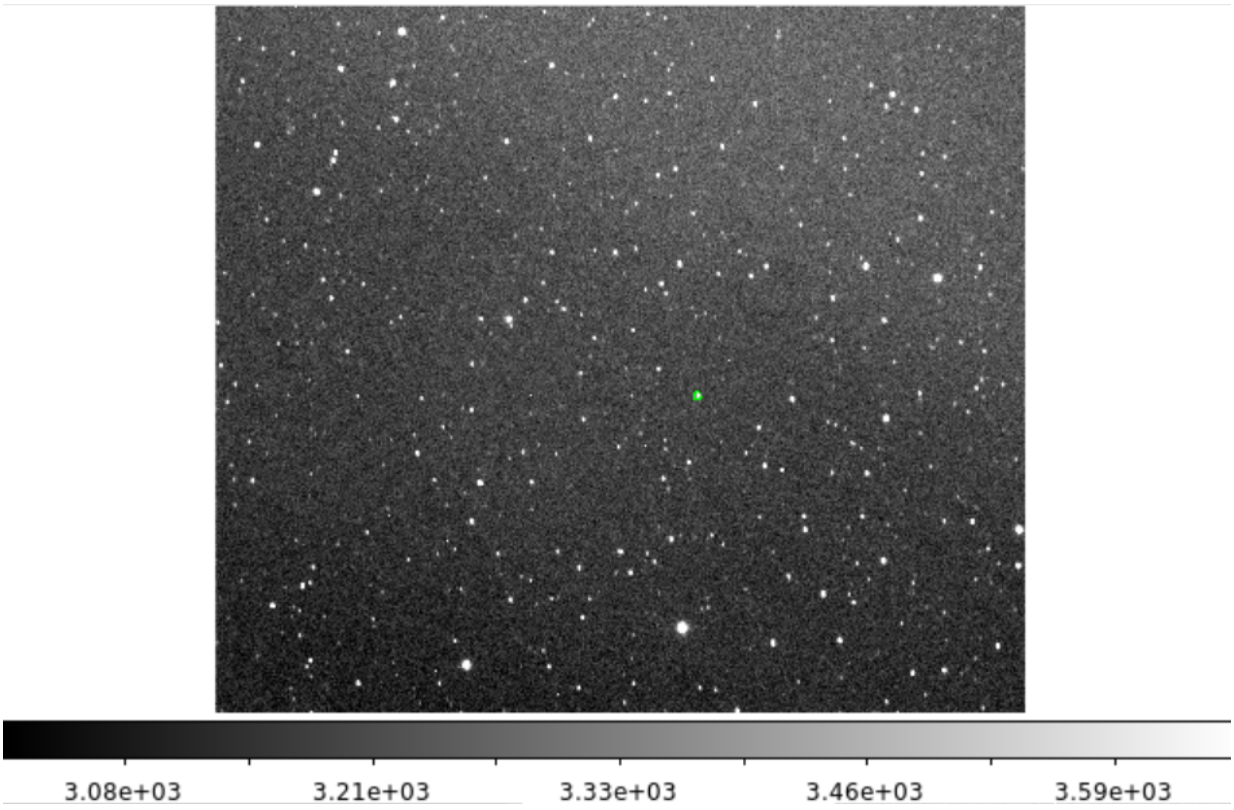

Figure 1. An image taken from the program DS9, where the green circle represents the fixed aperture that was used for Source Extractor. The host star is inside the fixed aperture. The fixed aperture was used to calculate the flux in every image.

Other than the host star, there were ten other stars selected to be the calibration stars needed for the experiment. A similar method was used to concatenate the images to create a table of time, flux, and flux error. The rest of the data reduction was done in Python.

After the time, flux, and flux error was obtained, a plot was made of the host star's flux vs. exposure time after the host star's flux and flux error were normalized by the average flux across all images. As seen in Fig. 2, there were many exposures that differed significantly from the other exposures. These exposures were removed from the data reduction of the host star and the reference stars. Without these exposures, a flux dip was evident in Fig. 3.

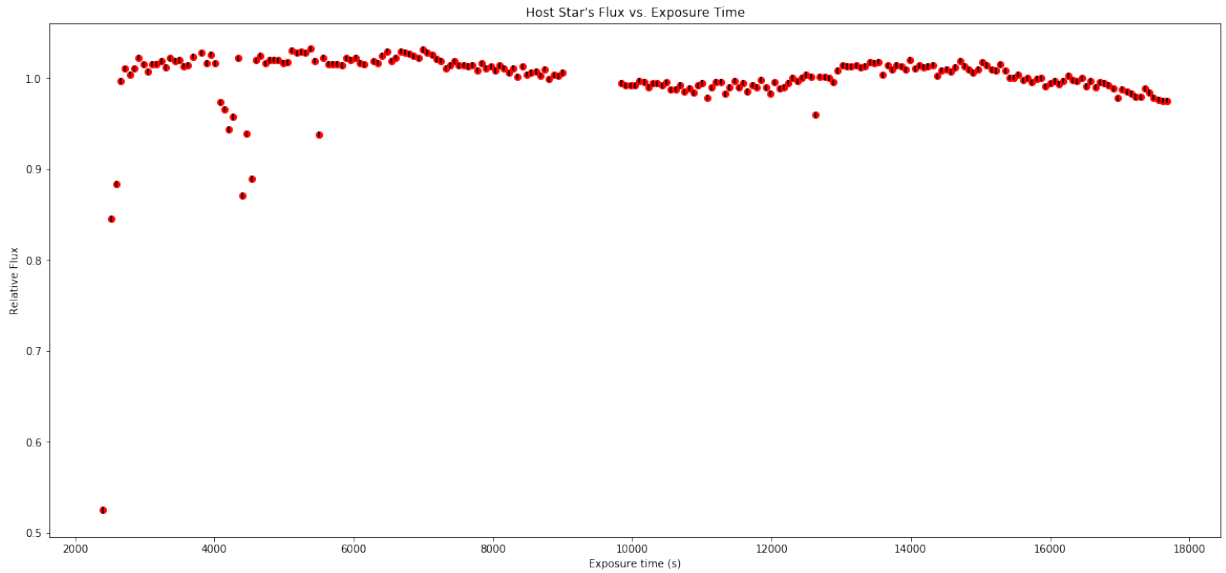

Figure 2. The plot of the host star's flux vs. exposure time. This plot shows the exposure times that are significantly different than the rest of the exposures.

The same method of normalization was applied to the reference stars, where the flux and flux error of each star for each image were normalized by the average flux across all images. As seen in Fig. 4, each reference star was plotted on the same plot, where each reference star's flux was added by a constant value to fit all of them on the same plot.

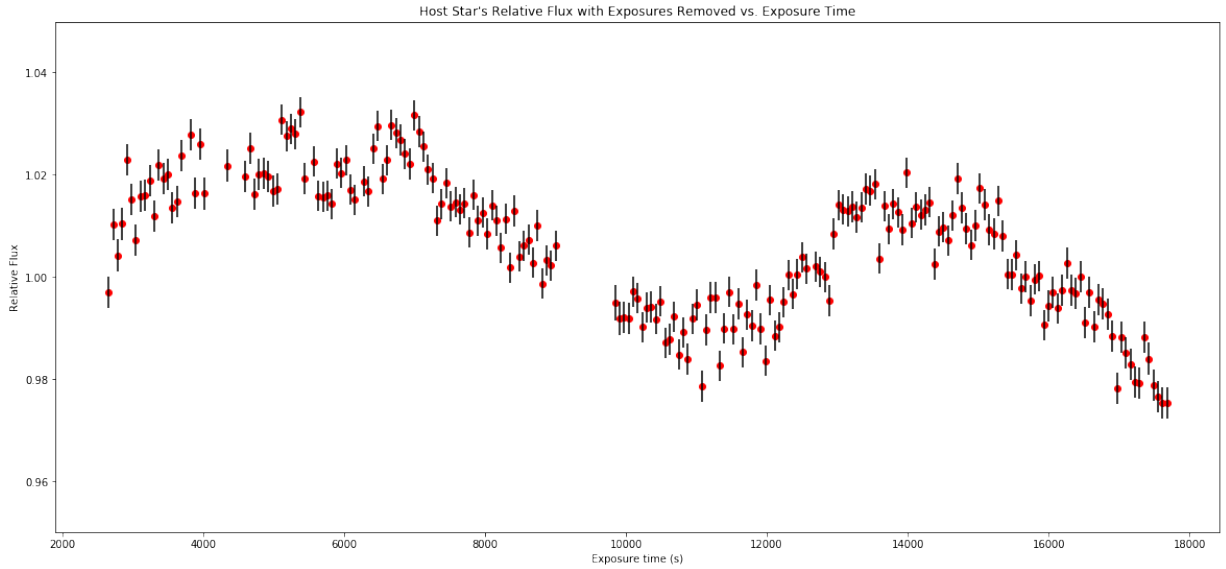

Figure 3. The plot of the host star's relative flux vs. exposure time. What is evident from this plot is that the exposures are removed compared to Fig. 2. A flux dip is evident from this plot as well.

Since atmospheric conditions can cause flux changes that are as large or larger than the flux we were trying to detect, we calculated the flux of the target stars relative to the flux of the reference stars. This accounted for the changes in the atmospheric conditions. This was done by averaging over the ten reference stars, which reduced the statistical noise as well as the systematic uncertainty from the variability in the reference stars.

To do this, the weighted mean was computed by using the equation

$$\mu_i^{ref} = \frac{\Sigma_j \frac{f_j^{ref}}{(\sigma_j^{ref})^2}}{\Sigma_j \frac{1}{(\sigma_j^{ref})^2}}. \tag{1}$$

The corresponding error on the weighted mean was

$$\sigma_j^{ref} = \left(\frac{1}{\frac{1}{(\Sigma_j \sigma_j^{ref})^2}} \right)^{1/2}, \tag{2}$$

where i was the subscript for each image and j represents each reference star. Using this, the ratio $r_i = \frac{f_i^{sci}}{\mu_i^{sci}}$ was found, where its error was

$$\sigma_r = r_i \left(\left(\frac{\sigma_{host}}{f_i^{sci}} \right)^2 + \left(\frac{\sigma_{mean}}{\mu_i^{ref}} \right)^2 \right)^{1/2}, \tag{3}$$

and this error was found by simple error propagation.

To normalize the ratio r_i, we divided it and its error by the baseline flux. The baseline flux was found by taking the flux before the transit started. Following that, the ratio r_i represented the fraction of light from the host star that is not obscured by the transiting exoplanet. The normalized flux was plotted against the exposure time in Fig. 5.

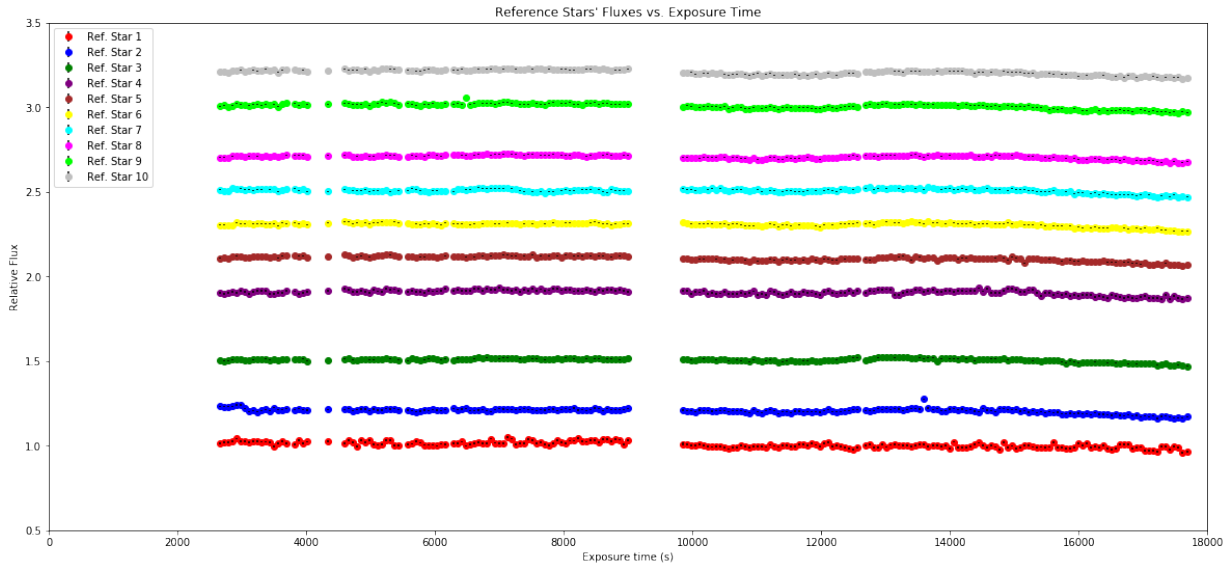

Figure 4. Ten reference stars plotted vs. exposure time. All of the reference stars were added by a constant so they would fit in one plot. The flat lines of each reference star tell you that there is not a lot of random variability between the exposures, allowing us to calibrate the host star with these reference stars.

4. DATA ANALYSIS

The baseline flux was found by taking the average of the flux values before the transit starts, which was before the blue vertical line in Fig. 5. The flux values after the end of the transit would have been taken into account as well;

however, it was unclear when the transit ended. So, the data was more accurate if only the flux values before the transit started were taken into account. The baseline flux value came out to be 1.0 ± 0.0004. The error of the baseline flux was found by finding the error of the mean baseline flux, which was equation

$$\sigma_{mean}^2 = \frac{1}{\Sigma_i \frac{1}{\sigma_i^2}}, \tag{4}$$

where i represents each image.

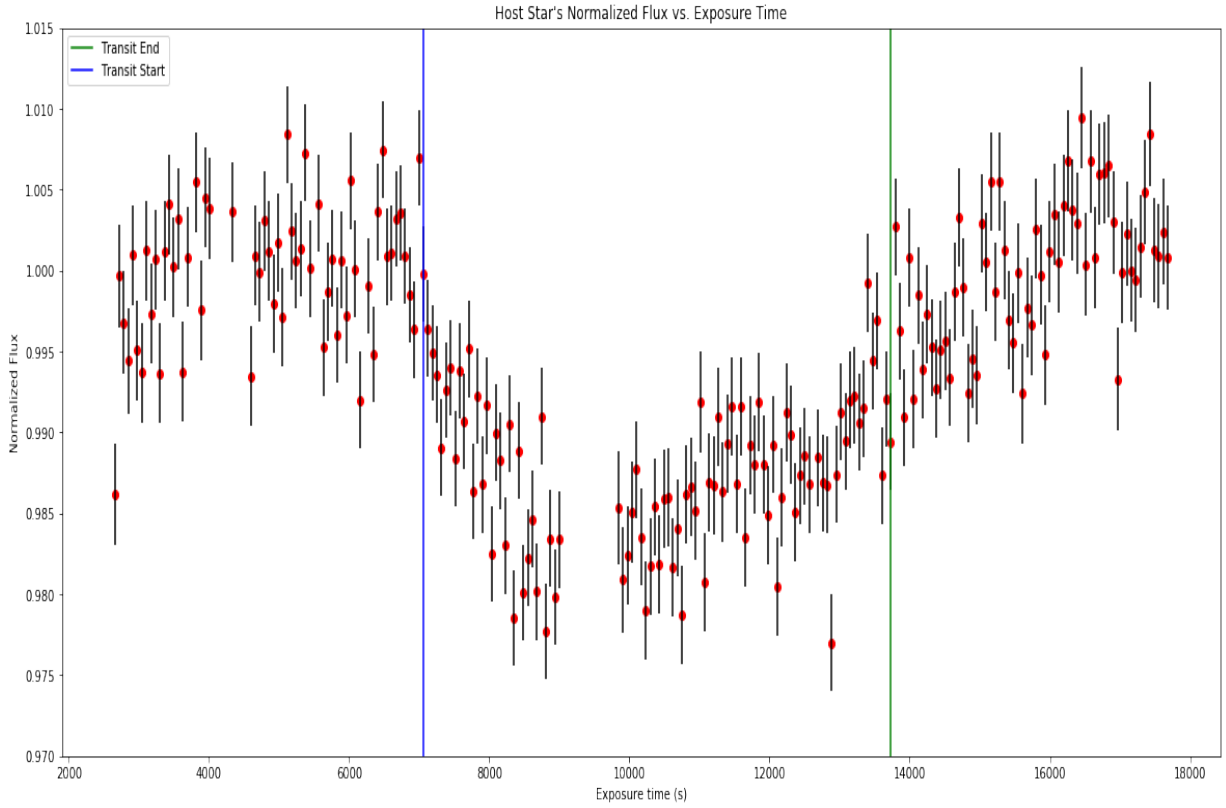

Figure 5. The host star's normalized flux plotted against exposure time. The blue vertical line represents the start of the transit, while the green vertical line represents the end of the transit. A transit depth is evident of at least 1.0 %.

The measurement of the transit flux was found by taking the average of the flux values between the two vertical lines shown in Fig. 5. The error of the transit flux was found by using Eqn. 4. The transit flux value came out to be 0.987 ± 0.0003.

The transit depth, which is the amount of blocked flux from the exoplanet transiting across the host star, was simply the average baseline flux subtracted by the average transit flux. The error of the transit depth was found by the simple error propagation formula

$$\sigma_{depth} = \sqrt{\sigma_{baseflux}^2 + \sigma_{transit}^2}. \tag{5}$$

The transit depth came out to be 1.27 % $\pm$ 0.0510 %.

Since the transit depth equation is

$$\delta_{depth} = \left(\frac{R_p}{R_{star}}\right)^2 = R^2, \tag{6}$$

where R_p is the radius of the transiting planet and R_{star} is the radius of the host star. This means that planet-to-star radius ratio is simply the square root of the transit depth. The error of the planet-to-star radius ratio is found by the

equations for single variable uncertainty:

$$\sigma_R = \frac{1}{2}\frac{\sigma_\delta}{\delta}R. \tag{7}$$

The planet-to-star radius ratio came out to be 0.113 ± 0.00200.

The last value that was found was the transit duration. This was found by subtracting the exposure time of the start of the transit by the exposure time of the end of the transit. The uncertainties of each time were found by how certain we were in where the transit started and where the transit ended. So, we chose about one exposure for the transit start since it is clear when the transit starts, where one exposure is equal to 60 seconds. For the end of the transit time, there was a lot more uncertainty for where the transit ended. So, we chose about seven exposures, which means that there was an error of around 420 seconds. Then, the uncertainty of was found the same way as the transit depth uncertainty. The transit duration came out to be 6671 seconds ± 424.3 seconds.

According to Bakos et al. (2011), the values they obtained are 1.36 % ± 0.007 % for the transit depth, 0.117 ± 0.001 for the planet-to-star radius ratio, and 7845 seconds ± 60.48 seconds for the transit duration. According to Tsantaki et al. (2014), the values they obtained are 1.46 % ± 0.007 % for the transit depth, 0.1209 ± 0.002 for the planet-to-star radius ratio, and 7102 seconds ± 69.12 seconds for the transit duration.

The statistical significance of our measurements compared to the literature values can be found by using the equation

$$\frac{|x_1 - x_2|}{\sqrt{(\sigma_{x_1}^2 + \sigma_{x_2}^2)}}, \tag{8}$$

where x_1 and x_2 are the measured and literature measurements, respectively, along with their corresponding errors. Our transit depth measurement has a significance level of 1.75σ and 3.69σ compared to Bakos et al. (2011) and Tsantaki et al. (2014)'s transit depth measurements, respectively. The planet-to-star radius ratio's measurement has a significance level of 1.79σ and 2.79σ compared to Bakos et al. (2011) and Tsantaki et al. (2014)'s measurement of the planet-to-star radius. Lastly, the transit duration measurement has a significance level of 2.74σ compared to Bakos et al. (2011)'s measurement and a significance level of 1.00σ compared to Tsantaki et al. (2014)'s measurement.

All of our measurements had a significance level under 3σ compared to literature values besides our transit depth measurement compared to Tsantaki et al. (2014)'s transit depth measurement. This means that the measurements that were taken in this experiment are more or less consistent with literature values measured by two different scientist collaborations. Therefore, it can be said that our measurements taken in this experiment are accurate as well, and they confirm the existence of the exoplanet Hat-P-23 b.

5. CONCLUSION

In this experiment, CCD images were taken of an extrasolar system called Hat-P-23. Data analysis of these images showed that there was an exoplanet transit that occurred during the observation. The transit depth came out to be 1.27 % ± 0.0510 %, the planet-to-star radius ratio came out to be 0.113 ± 0.00200, and the transit duration came out to be 6671 seconds ± 424.3 seconds. All of these measurements had a significance level under 3σ compared to the literature values from Bakos et al. (2011) and Tsantaki et al. (2014), besides the transit depth measurement from Tsantaki et al. (2014). Due to the relatively accurate results compared to literature values, it can be said that this report confirms the existence of the exoplanet Hat-P-23 b. The experiment could have been improved if there were multiple nights of observation that observed the exoplanet transit. Using the data from multiple nights, an average of them could have been created and this would have yielded more accurate results and reduce statistical and systematic uncertainties.

REFERENCES

Astrometry. 2019, Astrometry Website, http://astrometry.net/

Bakos, G. Á., Hartman, J., Torres, G., et al. 2011, ApJ, 742, 116, doi: 10.1088/0004-637X/742/2/116

CCD. 2019, CCD Manual, https://bit.ly/2m9BYHV

Charbonneau, D., Brown, T. M., Latham, D. W., & Mayor, M. 2000, ApJL, 529, L45, doi: 10.1086/312457

DS9. 2019, DS9 website, http://ds9.si.edu/site/Home.html

Gazak, J. Z., Johnson, J. A., Tonry, J., et al. 2012, Advances in Astronomy, 2012, 697967, doi: 10.1155/2012/697967

Meade. 2019, Meade Telescope Manual, http://www.meadeuk.com/pdf/lx200_acf_manual.pdf

PyRAF. 2019, PyRAF website, http://www.stsci.edu/institute/software_hardware/pyraf

SourceExtractor. 2019, Source Extractor Website, http://www.astromatic.net/software/sextractor

Tsantaki, M., Sousa, S. G., Santos, N. C., et al. 2014, A&A, 570, A80, doi: 10.1051/0004-6361/201424257